

Superconducting gaps revealed by STM measurements on $\text{La}_2\text{PrNi}_2\text{O}_7$ thin films at ambient pressure

Shengtai Fan^{1†}, Mengjun Ou^{1†}, Marius Scholten², Qing Li¹, Zhiyuan Shang¹, Yi Wang¹,
Jiasen Xu¹, Huan Yang^{1*}, Ilya M. Eremin^{2*}, Hai-Hu Wen^{1*}

¹ National Laboratory of Solid State Microstructures and Department of Physics, Jiangsu Physical Science Research Center, Collaborative Innovation Center of Advanced Microstructures, Nanjing University, Nanjing 210093, China.

² Institut für Theoretische Physik III, Ruhr-Universität Bochum, D-44801 Bochum, Germany

† These authors contribute equally to the work.

*Corresponding authors: huanyang@nju.edu.cn, Ilya.Eremin@ruhr-uni-bochum.de,
hhwen@nju.edu.cn

The recent discovery of superconductivity in nickelate systems has generated tremendous interests in the field of superconductivity. The superconducting transition temperature above 80 K in $\text{La}_3\text{Ni}_2\text{O}_7$ under pressure and the coexisting spin excitations certainly categorize the nickelate superconductors as unconventional. The core issue to understand the superconductivity mechanism is about the superconducting gap and its symmetry. By using the substrate of SrLaAlO_4 (001), we have successfully synthesized the superconducting thin film of $\text{La}_2\text{PrNi}_2\text{O}_7$ with $T_c^{\text{onset}} = 41.5$ K. Superconducting tunneling spectra are successfully measured on the terraces after we removed the surface layer and expose the superconducting layer by using the tip-excavation technique. The spectrum shows a two-gap structure with $\Delta_1 \approx 19$ meV, $\Delta_2 \approx$

6 meV, and fittings based on the Dynes model indicate that the dominant gap should have an anisotropic *s*-wave structure, and the pure *d*-wave model fails to fit the data. Thus, our data put the priority in selecting the s^{\pm} among the two arguable pairing models: s^{\pm} and *d*-wave. Assuming the dominant interlayer superconducting gap, we obtain its magnitude to be $\Delta_{\perp} \approx 13$ meV, while the intralayer gap is about $\Delta_{\parallel} \approx 6$ meV. Our results shed new light in understanding the mystery of superconductivity in bilayer nickelate superconductors.

Main

Superconductivity in nickelates opens up a new era in the research of unconventional high-temperature superconductivity. The starting point was from the observation of the superconductivity in the infinite-layer nickel-based $\text{Nd}_{1-x}\text{Sr}_x\text{NiO}_2$ and its sister compounds¹⁻² (for a review see Ref.3). Later on, the breakthrough in nickelate superconductors was the observation of high-temperature superconductivity with the onset transition temperature (T_c^{onset}) up to 80 K in bulk $\text{La}_3\text{Ni}_2\text{O}_7$ samples under the pressure above 14 GPa^{4,5}. Superconductivity under pressure has also been observed in the Ruddlesden-Popper bilayer $\text{La}_2\text{PrNi}_2\text{O}_7$ sample⁶ and $\text{La}_2\text{SmNi}_2\text{O}_{7-\delta}$ sample⁷, the trilayer $\text{La}_4\text{Ni}_3\text{O}_{10-\delta}$ samples⁸⁻¹⁰, as well as the $\text{La}_5\text{Ni}_3\text{O}_{11}$ sample¹¹. Recently, superconductivity with T_c^{onset} of about 40 K was observed at ambient pressure in the $\text{La}_3\text{Ni}_2\text{O}_7$ thin films¹², $(\text{La},\text{Pr})_3\text{Ni}_2\text{O}_7$ thin films¹³, and $\text{La}_{3-x}\text{Sr}_x\text{Ni}_2\text{O}_7$ thin films¹⁴ with an in-plane strain, which opens a new chapter of the research on high-temperature superconductivity in nickelates at ambient pressure.

The observation of superconductivity in nickelate superconductors inspires scientists to investigate the electronic structure and the superconducting mechanism, especially in the Ruddlesden-Popper (RP) 327 system that holds the high- T_c superconductivity. The angle-resolved photoemission spectroscopic (ARPES) measurements reveal the band structure in $\text{La}_3\text{Ni}_2\text{O}_7$ at ambient pressure, i.e., the α and β pockets are mainly contributed by the $3d_{x^2-y^2}$ orbital with some hybridization of the $3d_{z^2}$ orbital, and a flat bonding γ -band is derived from the $3d_{z^2}$ orbital which may exceed or lie just below the Fermi level^{15,16}. Under high pressure, the bonding γ band may cross the Fermi energy, which was argued to be closely related to the high- T_c superconductivity^{4,17-31}. This is different from cuprates in which the dominant contribution to superconductivity comes from the $3d_{x^2-y^2}$ band. However, it remains controversial whether the γ pocket is absent³² or blurred³³ in the 327 strained thin films, which makes the origin of high- T_c superconductivity more complex and interesting. According to the

varieties of theoretical models, they may be categorized into two major camps for the superconducting pairing symmetry for pressured 327 bulks. The first one supports the so-called s^\pm -wave^{19,20,27-31} scenario in which the Cooper-pairing appears as a result of the dominant interlayer interaction with dominant interlayer gap Δ_\perp and a smaller intralayer component Δ_\parallel which results from the intralayer interaction. The gap is then positive, $\Delta_\perp + \Delta_\parallel$ on the symmetric (bonding) band and negative $\Delta_\parallel - \Delta_\perp$ on the antisymmetric (antibonding) band. In the second scenario the dominant in-plane repulsive interaction due to antiferromagnetic spin fluctuations drives the d -wave symmetry of the superconducting state^{28,29,34-36}, which is somewhat similar to the cuprates. However, the experimental data supporting any gap symmetry is rare because of the very high pressure to achieve superconductivity, besides a preliminary study by using the Andreev reflection under pressure in $\text{La}_3\text{Ni}_2\text{O}_7$ ³⁷, and therefore, high-quality experimental data for showing the gap structure and intimately pinning down the superconducting mechanism are highly desired. Thanks to the discovery of superconductivity in 327 films with high- T_c superconductivity at ambient pressure, it is now possible to measure the gap structure by using the commonly used tools, such as the scanning tunneling microscopy and spectroscopy (STM/STS).

In this work, we report the successful growth of the $\text{La}_2\text{PrNi}_2\text{O}_7$ thin films with T_c^{onset} up to 41.5 K. We successfully carried out the STM/STS measurements on the film, and obtained the tunneling spectra in the superconducting region constructed by the tip-excavation technique. The fitting results strongly suggest the dominance of anisotropic s -wave gap(s) in the film, supporting the Cooper-pairing scenario of s^\pm . These results provide key information in understanding the superconducting mechanism in superconducting $\text{La}_2\text{PrNi}_2\text{O}_7$ thin films.

Superconductivity in $\text{La}_2\text{PrNi}_2\text{O}_7$ films

The 2-unit-cell (2UC) $\text{La}_2\text{PrNi}_2\text{O}_7$ thin films were grown by pulsed laser deposition on (001)-oriented SrLaAlO_4 substrates with an in-situ ozone annealing process (see Methods for details). To check the superconducting properties of the prepared 2UC $\text{La}_2\text{PrNi}_2\text{O}_7$ thin films, we perform the low temperature transport measurement and show the results in Fig. 1a-c and Extended Data Fig. 1. Temperature dependent resistivity of $\text{La}_2\text{PrNi}_2\text{O}_7$ thin film shows good metallic behavior and a clear superconducting transition. The onset transition temperature defined by the cross point of the red lines in the inset of Fig. 1a is about 41.5 K, and this value is comparable to the previous reported values of T_c on bilayer nickelate strained thin films. The value of resistivity is close to zero at 2 K, showing a relatively broad transition. This does not prevent us from measuring valid tunneling spectrum concerning superconductivity since it is a very local tool. Figure 1b and Extended Data Fig. 1 show the magneto-transport measurements on a $\text{La}_2\text{PrNi}_2\text{O}_7$ thin film with applied magnetic field along ($H // c$) and perpendicular to ($H \perp c$) the c axis, respectively. The superconducting transition is gradually suppressed, and the transition temperature shows a strong anisotropic response under magnetic fields. Figure 1c shows the temperature dependent out-of-plane and in-plane upper critical fields ($\mu_0 H_{c2}$) with criteria of 90% and 50% normal-state resistivity $\rho_n(T)$. All the data can be well fitted by the Ginzburg-Landau (GL) model. The fitting yields the zero-temperature upper critical fields 118 and 43 T for the criteria of 90% and 50% when $H \perp c$, and 153 and 80 T for 90% and 50% when $H // c$, respectively.

Figure 1d shows the X-ray diffraction (XRD) 2θ - ω scans of our $\text{La}_2\text{PrNi}_2\text{O}_7$ thin film and the SrLaAlO_4 substrate. All the (00 l) peaks can be well indexed by the bilayer structure, and there is no signature of impurity phases. The tiny peaks marked with asterisks are found to be induced by the substrate since they appear even with the bare substrate (shown at the bottom of Fig. 1d). The c -axis lattice constant calculated from the XRD data is about 20.78 Å

which is about 1% elongated compared to bulk sample⁶ and in good agreement with the previous reported thin films¹³. The surface morphological features of the thin films are checked by Atomic Force Microscopy (AFM) and STM. As shown in Fig. 1e, the AFM data measured at room temperature give a root-mean-square roughness of the La₂PrNi₂O₇ thin film surface of about 220 pm.

Superconducting region obtained by STM tip

The surfaces of the thin films are rather flat as viewed by the AFM measurements, specifically with a surface root-mean-square roughness of about 0.2 nm, but the local fluctuation can be larger than 1 nm. In addition, the films were exposed to the air after growth in the PLD chamber, and they were transferred to the STM/STS chamber to carry out the tunneling measurements. Therefore, the surfaces of the films are somewhat degenerated and may also be contaminated when exposed to air, thus showing some kind of disorder on the nanometer scale. An example is shown in Fig. 1f, where one can see that the surface shows a background with some grains, and the roughness is in the scale of 1-3 nm. The calculated root-mean-square roughness is about 0.67 nm, which is a challenge for the measurements of atomically resolved scanning tunneling spectra. In order to get a fresh surface, we try to use the tip-excavation technology³⁸, i.e., applying a bias pulse of 2 V to the tip when it is stabilized in the initial setpoint conditions of $V_{\text{set}} = 8$ V and $I_{\text{set}} = 20$ pA. The pulse may cause an abrupt change in the distance between the tip and the film and take away some part of the film. The topographic image before and after the treatment is shown in Extended Data Fig. 2a and Fig. 2a (or Fig. 2c and Extended Data Fig. 2b), respectively. One can see that a large part of the covered film and even the top atomic layers of the substrate have been removed by the tip-excavation process. The nature of the substrate is confirmed by the tunneling spectrum which show a very large insulating gap (Extended Data Fig. 2c).

Because of the elimination of some atomic layers of the substrate, the height difference between the film surface and the substrate can be as large as about 11 nm, which is derived from the spatial dependence of height shown in Fig. 2b. This value seems larger than the film thickness of 4 nm (2UC), which suggests that some layers of the substrate has also been removed.

Then, we carried out the tunneling spectrum measurements on the inner layer of the film which is exposed by the tip-excavation technique, i.e., the superconducting (SC) layer 1 as illustrated in Fig. 2a. A set of tunneling spectra measured along the arrowed line on SC layer 1 and at 1.8 K is shown in Fig. 2d. All the spectra show superconducting shapes with coherence-peak features appearing at around ± 20 meV. Meanwhile, there are some kink structures appearing at about $\pm 6 \sim \pm 10$ meV, which can be related to another smaller superconducting gap. We should emphasize that the features of the spectra are very similar to each other, therefore, the two-gap feature is a common one on SC layer 1. However, the coherence-peak feature becomes very weak on the spectra measured on the surface layer (SC layer 2), although the gap feature at 20 meV is still quite clear (Extended Data Fig. 2d), which may be due to the oxygen loss of the surface layers¹³.

Characterization of the superconducting gap

In order to confirm that the gapped feature is from superconductivity, we carried out the spectrum measurement at different temperatures, and the results are shown in Fig. 3a. With the increase of temperature, the coherence peak feature at about ± 20 meV is suppressed while the differential conductance at zero bias is lifted up. The gapped feature almost disappears on the spectrum measured at about 30 K, which is the T_c derived from the criterion of $50\% \rho_n(T)$. Therefore, we believe the gapped feature is from superconductivity. We use the spectrum measured at 30 K as the background and normalize the spectra

measured at other temperatures, and the result is shown in Fig. 3b. One can see that the spectra show a better particle-hole symmetric behavior after being normalized by the data measured at 30 K.

The spectra show a generally gapped feature below about 20 meV; meanwhile, the spectrum shape behaves somewhat like a “V” shape near zero bias (corresponding to the smaller gap). Usually, the V-shaped spectrum near zero bias is a signature of a nodal gap. For example, the observation of a V-shaped spectrum in $\text{Nd}_{1-x}\text{Sr}_x\text{NiO}_2$ thin films corresponds to a dominant nodal *d*-wave gap in the material from our previous work³⁷. In order to get a comprehensive understanding of the gap structure, we carried out carefully fitting based on the Dynes model³⁹. Although the gap energies are symmetric and spatially rather uniform (Fig. 2d), the spectrum shows a clear particle-hole asymmetric behavior. This could be induced by the normal state background or the correlation effect^{15,16,40,41} (see Supplementary Materials). In order to have a valid comparison with the theoretical fitting curves, we first normalize the spectrum measured at 1.8 K with the one measured at 30 K, the asymmetry becomes clearly weaker. But one can still see a declined background towards the positive bias; then we further normalize the data with an inclined background (Extended Data Fig. 3), making the spectrum more symmetric. The obtained spectrum shows almost particle-hole symmetric behavior. We must emphasize that all these treatments do not have a significant influence on the gap values and the spectrum of the negative bias. Since there is an obvious two-gap feature on the spectrum, we use the two-gap Dynes model³⁹ with different gap functions to fit the normalized spectrum, and the results are shown in Figs. 3c-3e. We first try the fitting with two components, each has an anisotropic *s*-wave gap. The fitting curve together with the normalized data is shown in Fig. 3c, and one can see that the data can be nicely fitted with $\Delta_1 = 19 \times (0.17 \cos 4\theta + 0.83)$ meV and $\Delta_2 = 6 \times (0.2 \cos 4\theta + 0.8)$ meV with a weight of 65% for the larger gap. Then we used an anisotropic *s*-wave gap for the

larger one, and a d -wave gap for the smaller one; the used gap functions are $\Delta_1 = 18.5 \times (0.18 \cos 4\theta + 0.82)$ meV and $\Delta_2 = 5.5 \cos 2\theta$ meV. Now the weight for the larger gap is about 70%. The results are shown in Fig. 3d. We must say the fitting has the same quality as the one by using two anisotropic s -wave gaps. However, if we use a model with two d -wave components, it is impossible to get any reasonable fit by tuning all parameters. The best fit by using two d -wave gaps is shown in Fig. 3e, here we use the two gaps $\Delta_1 = 19 \cos 2\theta$ meV and $\Delta_2 = 6 \cos 2\theta$ meV. The main difficulty is that if a d -wave gap is taken for the larger gap value around 20 meV, it has no way to fit the global shape of the spectrum, and the kink corresponding to the small gap is completely smeared out. The parameters for all fittings mentioned above are given in Extended Data Table I.

Discussion and comparison with theory

As shown above, in the superconducting $\text{La}_2\text{PrNi}_2\text{O}_7$ films, we have observed that the dominant gap (~ 19 meV) should be s -wave with some anisotropy. The smaller gap (~ 6 -7 meV) should also have anisotropy and it is discernable whether it is an anisotropic s -wave gap (probably with accidental nodes) or a d -wave gap. Actually, the dominant gap is the most important factor to decide which pairing model is really functioning in the system. We start to discuss this issue by taking a simplified three-band model. For the NiO_2 -bilayer system, the low-energy electronic structure is typically described by the low-energy effective model consisting of two $3d_{x^2-y^2}$ and $3d_{z^2}$ -orbitals located on two sites in a bilayer¹⁷, as shown in Fig. 4a. Introducing bonding-antibonding combinations of the orbitals the normal state Hamiltonian can be diagonalized and according to the DFT results¹⁷ there are three α , β , and γ bands, which cross the Fermi level. Within bonding-antibonding classification α -, and γ -bands can be characterized as bonding bands of mostly $3d_{x^2-y^2}$ and $3d_{z^2}$ -orbital character at the Fermi level, respectively, while β -band is an antibonding one with $3d_{x^2-y^2}$ -mostly

orbital-character at the Fermi surface, these three bands are schematically shown in Figs. 4b and 4c. Note the antibonding $3d_{z^2}$ – mostly orbital band appears to be well above the Fermi level⁴². In addition, the exact position of the γ -band with respect to the Fermi level and its classification is not fully settled both experimentally^{32,42} and theoretically⁴³. In what follows we however ignore its presence taking as an excuse for the fact that experimentally we see the signatures of only two superconducting gaps and thus restrict ourselves to α and β -bands only. Note that this is only an approximation and whether or not γ -band participates in the superconductivity cannot be solved within our study as our results are not momentum resolved.

Having only bonding-antibonding α and β bands simplifies the analysis significantly. The superconducting gaps can be characterized by the intralayer gaps $\Delta_{||}(\mathbf{k})$ driven by the intralayer magnetic fluctuations and the interlayer gaps, $\Delta_{\perp}(\mathbf{k})$, driven by the interlayer magnetic fluctuations. Overall, the superconducting state can be described by the following generic 4×4 Hamiltonian matrix in the Nambu-Gor'kov basis:

$$\hat{H}_{SC} = \Phi^{\dagger} \begin{pmatrix} \varepsilon_{||}(\mathbf{k}) & t_{\perp}(\mathbf{k}) & \Delta_{||}(\mathbf{k}) & \Delta_{\perp}(\mathbf{k}) \\ t_{\perp}(\mathbf{k}) & \varepsilon_{||}(\mathbf{k}) & \Delta_{\perp}(\mathbf{k}) & \Delta_{||}(\mathbf{k}) \\ \Delta_{||}(\mathbf{k}) & \Delta_{\perp}(\mathbf{k}) & -\varepsilon_{||}(\mathbf{k}) & -t_{\perp}(\mathbf{k}) \\ \Delta_{\perp}(\mathbf{k}) & \Delta_{||}(\mathbf{k}) & -t_{\perp}(\mathbf{k}) & -\varepsilon_{||}(\mathbf{k}) \end{pmatrix} \Phi, \quad (1)$$

where $\Phi = (c_{1,k\uparrow}, c_{2,k\uparrow}, c_{1-k\downarrow}^{\dagger}, c_{2-k\downarrow}^{\dagger})$ are the second quantization operators of layers 1 and 2, $\varepsilon_{||}(\mathbf{k})$ is the in-plane dispersion and $t_{\perp}(\mathbf{k})$ is the interlayer hybridization. Most importantly, Eq. (1) can be diagonalized by transforming the basis into bonding-antibonding one with respect to the layer index $c_{\alpha,k\uparrow} = \frac{1}{\sqrt{2}}(c_{1,k\uparrow} + c_{2,k\uparrow})$ and $c_{\beta,k\uparrow} = \frac{1}{\sqrt{2}}(c_{1,k\uparrow} - c_{2,k\uparrow})$ and the eigenenergies decompose into $E_{\alpha}(\mathbf{k}) = \pm \sqrt{(\varepsilon_{\alpha}(\mathbf{k}))^2 + (\Delta_{\alpha}(\mathbf{k}))^2}$ and $E_{\beta}(\mathbf{k}) = \pm \sqrt{(\varepsilon_{\beta}(\mathbf{k}))^2 + (\Delta_{\beta}(\mathbf{k}))^2}$ where $\varepsilon_{\alpha}(\mathbf{k})$ and $\varepsilon_{\beta}(\mathbf{k})$ refer to the α and β bands, which give rise to the α and β Fermi surfaces in the normal state. Most importantly, the gap on the α band is given by $\Delta_{\alpha}(\mathbf{k}) =$

$\Delta_{||}(\mathbf{k}) + \Delta_{\perp}(\mathbf{k})$ and on the β band $\Delta_{\beta}(\mathbf{k}) = \Delta_{||}(\mathbf{k}) - \Delta_{\perp}(\mathbf{k})$. For further analysis we recall that the most common candidate solutions for the superconducting gap in the bilayer nickelates, discussed in the literature, are either sign-changing bonding-antibonding s_{\pm} -wave symmetry or d -wave (either d_{xy} or $d_{x^2-y^2}$) symmetry solutions²⁸, as illustrated in Fig. 4b and 4c. For the s^{\pm} -wave symmetry solution, it is important that the interlayer gap is larger in magnitude than the intralayer one, i.e. superconductivity is driven by the interlayer spin fluctuations. We further assume Δ_{\perp} to be momentum independent, while $\Delta_{||}^s(\mathbf{k}) = \frac{\Delta_{s,||}^0}{2}(\cos k_x + \cos k_y)$. Depending on $\Delta_{s,||}^0$ magnitude the gaps on α and β bands become anisotropic and may even acquire accidental nodes if intralayer and interlayer gaps become of the same order.

In the case of the d -wave symmetry, it is expected that these are derived from intralayer spin fluctuations, which mostly drive the Cooper-pairing. We proceed by assuming $d_{x^2-y^2}$ -wave symmetry for concreteness yet d_{xy} -wave gives similar results. The intralayer gap is then $\Delta_{||}^d(\mathbf{k}) = \frac{\Delta_{d,||}^0}{2}(\cos k_x - \cos k_y)$ and by symmetry arguments the interlayer gap should also acquire the d -wave form factor, i.e. $\Delta_{\perp}^d(\mathbf{k}) = \frac{\Delta_{d,\perp}^0}{2}(\cos k_x - \cos k_y)$ and $\Delta_{d,||}^0 > \Delta_{d,\perp}^0$. Most importantly the non-zero $\Delta_{d,\perp}^0$ value yields different magnitude gaps on the α and β Fermi surface sheets but do not introduce any additional anisotropy. The latter would in principle appear if one introduces higher in-plane harmonics of the d -wave symmetry.

Keeping in mind that the superconducting gaps can be treated independently on two different bands, we thus proceed with fitting the experimental data using the Dynes formula with two gaps assuming three different scenarios: (i) two anisotropic s -wave gaps of different magnitudes, (ii) one anisotropic s -wave and one d -wave gaps of different magnitudes, and (iii) two d -wave superconducting gaps of different magnitudes, as proposed in some models^{44,45}. Our fitting to the experimental data, as discussed above, clearly indicates that the third case, namely the global d -wave gap cannot be fitted to experimental data. As our

experimental data support the dominance of anisotropic s -wave gaps in the present system, we can estimate the sizes of the interlayer and intralayer gaps. Assuming that Δ_1 and Δ_2 have opposite signs, we obtain the magnitude of the interlayer gap to be $\Delta_{\perp} \approx 13$ meV, while the intralayer gap is $\Delta_{\parallel} \approx 6$ meV. This can be taken as an estimate of the strength of the interlayer and intralayer spin fluctuations, respectively. We note, however, that the overall conclusion on the sign-changing bonding-antibonding s_{\pm} -wave symmetry needs to be verified by momentum resolved measurements in future experiments. In addition, the superconducting transition T_c^{onset} is about 41.5 K in the present sample, which is still below the highest value reported for the system under pressure. Thus, it may be subject to some modifications in the future for samples with optimized superconductivity. Our present results give strong evidence that the dominant superconducting gap is induced by the interlayer pairing even without the involvement of the γ Fermi pocket.

Methods

Film growth and characterization

The 2-unit-cell $\text{La}_2\text{PrNi}_2\text{O}_7$ thin films were epitaxially grown on single-crystal SrLaAlO_4 (001) substrates by pulsed laser deposition (PLD) using a KrF excimer laser ($\lambda = 248$ nm). A polycrystalline $\text{La}_2\text{PrNi}_2\text{O}_7$ target, prepared via the sol-gel method, was ablated at a laser fluence of 1.2-1.4 J/cm² with a repetition rate of 2 Hz. The deposition was performed at 780°C under an oxygen partial pressure of 20 Pa. Following deposition, the sample temperature was cooled to 550°C at a controlled rate of 10°C/min in the same oxygen atmosphere. The samples were maintained at 550°C and then post-annealed with ~7 wt% ozone for 30 minutes. The ozone was delivered through a nozzle positioned 1.8 cm from the sample surface, with the partial pressure and flow rate precisely maintained at 20 Pa and 10 sccm, respectively. After ozone treatment, the temperature was cooled down to 250°C at a rate of 15°C/min, after

which the ozone supply was turned off while maintaining the chamber pressure for natural cooling. The electrical transport properties were characterized using the standard four-probe method in a Physical Property Measurement System (PPMS, Quantum Design). Structural characterization was performed using a Bruker D8 Advanced X-ray diffractometer, and surface morphology was investigated by atomic force microscopy (FM-Nanoview6800).

STM/STS measurements

The STM/STS measurements were carried out in a scanning tunneling microscope (USM-1300, Unisoku Co., Ltd.) with ultra-high vacuum, low temperature, and high magnetic field. The thin films were transferred to the STM head across the high-vacuum chamber as soon as possible. The electrochemically etched tungsten tips were used for the STM/STS measurements. A typical lock-in technique was used for the tunneling spectrum measurements with an ac modulation of 1% of V_{set} and 931.773 Hz. Unless otherwise specified, the setpoint conditions for the tunneling spectrum measurements are: $V_{\text{set}} = 50$ mV and $I_{\text{set}} = 100$ pA.

Dynes model fitting

Based on the Dynes model, we describe the differential conductance as,

$$G(V) \propto \frac{d}{dV} \left(\int_{-\infty}^{+\infty} d\varepsilon \int_0^{2\pi} d\theta [f(\varepsilon) - f(\varepsilon + eV)] \cdot \text{Re} \left(\frac{\varepsilon + eV + i\Gamma}{\sqrt{(\varepsilon + eV + i\Gamma)^2 - \Delta^2(\theta)}} \right) \right) \quad (2)$$

where $f(\varepsilon)$ is the fermi distribution function, Δ denotes the superconducting gap value, and Γ represents the scattering factor assumed to be isotropic. The spectra are fitted by the Dynes model³⁹ with two isolated superconducting gaps. In this situation, the total differential conductance can be expressed as $G = xG_1 + (1-x)G_2$, where G_1 or G_2 is the differential conductance contributed by the gap Δ_1 or Δ_2 , and x or $1-x$ is the spectral weight contributed by the gap Δ_1 or Δ_2 . All parameters used for fitting are summarized in Extended Data Table I.

Data availability

The data that support the findings of this study are available from the corresponding authors upon reasonable request.

Acknowledgements

We appreciate the useful discussions with Harold Hwang in Stanford university and Daoxin Yao in Sun Yat-Sen university. This work is supported by the National Key R&D Program of China (Grant No. 2022YFA1403201 and No. 2024YFA1408104), the Natural Science Foundation of China (Grant No. 12494591, No. 11927809 and No. 12434004), and the Natural Science Foundation of Jiangsu Province (Grant No. BK20233001).

Author contributions

The $\text{La}_2\text{PrNi}_2\text{O}_7$ thin films were grown and characterized by M.O., Q.L., Y.W., and H.-H.W. The STM measurements and data analysis were done by S.F., Z.S., J.X., H.Y., and H.H.W. Theoretical calculations were carried out by M.S. and I.E. The manuscript was written by S.F., Q.L., H.Y., I.E., and H.-H.W., which is supplemented by others. H.-H.W. has coordinated the whole work.

Competing interests

The authors declare no competing interests.

References

1. Li, D. et al. Superconductivity in an infinite-layer nickelate. *Nature* **572**, 624–627 (2019).
2. Zeng, S. et al. Phase diagram and superconducting dome of infinite-layer $\text{Nd}_{1-x}\text{Sr}_x\text{NiO}_2$

- thin films. *Phys. Rev. Lett.* **125** 147003 (2020).
3. Gu, Q. & Wen, H.-H. Superconductivity in nickel-based 112 systems. *Innovation* **3**, 100202 (2022).
 4. Sun, H. et al. Signatures of superconductivity near 80 K in a nickelate under high pressure. *Nature* **621**, 493-498 (2023).
 5. Zhang, Y. et al. High-temperature superconductivity with zero resistance and strange-metal behaviour in $\text{La}_3\text{Ni}_2\text{O}_{7-\delta}$. *Nat. Phys.* **20**, 1269-1273 (2024).
 6. Wang, N. et al. Bulk high-temperature superconductivity in pressurized tetragonal $\text{La}_2\text{PrNi}_2\text{O}_7$. *Nature* **634**, 579-584 (2024).
 7. Li, F. et al. Ambient pressure growth of bilayer nickelate single crystals with superconductivity over 90 K under high pressure. Preprint at <https://arxiv.org/abs/2501.14584> (2025).
 8. Zhu, Y. et al. Superconductivity in pressurized trilayer $\text{La}_4\text{Ni}_3\text{O}_{10-\delta}$ single crystals. *Nature* **631**, 531-536 (2024).
 9. Li, Q. et al. Signature of superconductivity in pressurized $\text{La}_4\text{Ni}_3\text{O}_{10}$. *Chin. Phys. Lett.* **41**, 017401 (2024).
 10. Sakakibara, H. Theoretical analysis on the possibility of superconductivity in the trilayer Ruddlesden-Popper nickelate $\text{La}_4\text{Ni}_3\text{O}_{10}$ under pressure and its experimental examination: Comparison with $\text{La}_3\text{Ni}_2\text{O}_7$. *Phys. Rev. B* **109**, 144511 (2024).
 11. Shi, M. et al. Superconductivity of the hybrid Ruddlesden-Popper $\text{La}_5\text{Ni}_3\text{O}_{11}$ single crystals under high pressure. Preprint at <https://arxiv.org/abs/2502.01018> (2025).
 12. Ko, E. K. et al. Signatures of ambient pressure superconductivity in thin film $\text{La}_3\text{Ni}_2\text{O}_7$. *Nature* **638**, 935-940 (2025).
 13. Zhou, G. et al. Ambient-pressure superconductivity onset above 40 K in $(\text{La},\text{Pr})_3\text{Ni}_2\text{O}_7$ films. *Nature* **640**, 641-646 (2025).

14. Bao, B., et al. Superconductivity and phase diagram in Sr-doped $\text{La}_3\text{Ni}_2\text{O}_7$ thin films. Preprint at <https://arxiv.org/abs/2505.12603> (2025).
15. Yang, J. et al. Orbital-dependent electron correlation in double-layer nickelate $\text{La}_3\text{Ni}_2\text{O}_7$. *Nat. Commun.* **15**, 4373 (2024).
16. Abadi, S. Electronic structure of the alternating monolayer-trilayer phase of $\text{La}_3\text{Ni}_2\text{O}_7$. *Phys. Rev. Lett.* **134**, 126001 (2025).
17. Luo, Z., Hu, X., Wang, M., Wú, W. & Yao, D. X. Bilayer two-orbital model of $\text{La}_3\text{Ni}_2\text{O}_7$ under pressure. *Phys. Rev. Lett.* **131**, 126001 (2023).
18. Zhang, Y., Lin, L. F., Moreo, A. & Dagotto, E. Electronic structure, dimer physics, orbital-selective behavior, and magnetic tendencies in the bilayer nickelate superconductor $\text{La}_3\text{Ni}_2\text{O}_7$ under pressure. *Phys. Rev. B* **108**, L180510 (2023).
19. Yang, Q. G., Wang, D. & Wang, Q. H. Possible s_{\pm} -wave superconductivity in $\text{La}_3\text{Ni}_2\text{O}_7$. *Phys. Rev. B* **108**, L140505 (2023).
20. Shen, Y., Qin, M. & Zhang, G. M. Effective bi-layer model Hamiltonian and density-matrix renormalization group study for the high- T_c superconductivity in $\text{La}_3\text{Ni}_2\text{O}_7$ under high pressure. *Chin. Phys. Lett.* **40**, 127401 (2023).
21. Lechermann, F., Gondolf, J., Bötzel, S. & Eremin, I. M. Electronic correlations and superconducting instability in $\text{La}_3\text{Ni}_2\text{O}_7$ under high pressure. *Phys. Rev. B* **108**, L201121 (2023).
22. Qin, Q. & Yang, Y. F. High- T_c superconductivity by mobilizing local spin singlets and possible route to higher T_c in pressurized $\text{La}_3\text{Ni}_2\text{O}_7$. *Phys. Rev. B* **108**, L140504 (2023).
23. Christiansson, V., Petocchi, F. & Werner, P. Correlated electronic structure of $\text{La}_3\text{Ni}_2\text{O}_7$ under pressure. *Phys. Rev. Lett.* **131**, 206501 (2023).
24. Yang, Y. F., Zhang, G. M. & Zhang, F. C. Interlayer valence bonds and two-component theory for high- T_c superconductivity of $\text{La}_3\text{Ni}_2\text{O}_7$ under pressure. *Phys. Rev. B* **108**,

L201108 (2023).

25. Liu, Y. B., Mei, J. W., Ye, F., Chen, W. Q. & Yang, F. s^{\pm} -wave pairing and the destructive role of apical-oxygen deficiencies in $\text{La}_3\text{Ni}_2\text{O}_7$ under pressure. *Phys. Rev. Lett.* **131**, 236002 (2023).
26. Luo, Z., Lv, B., Wang, M., Wú, W. & Yao, D.-X. High- T_C superconductivity in $\text{La}_3\text{Ni}_2\text{O}_7$ based on the bilayer two-orbital t-J model. *npj Quan. Mater.* **9**, 61 (2024).
27. Ouyang, Z., Gao, M. & Lu, Z. Y. Absence of electron-phonon coupling superconductivity in the bilayer phase of $\text{La}_3\text{Ni}_2\text{O}_7$ under pressure. *npj Quan. Mater.* **9**, 80 (2024).
28. Bötzel, S., Lechermann, F., Gondolf, J. & Eremin, I. M. Theory of magnetic excitations in the multilayer nickelate superconductor. *Phys. Rev. B* **109**, L180502 (2024).
29. Xi, W., Yu, S.-L. & Li, J.-X., Transition from s_{\pm} -wave to $d_{x^2-y^2}$ -wave superconductivity driven by interlayer interaction in the bilayer two-orbital model of $\text{La}_3\text{Ni}_2\text{O}_7$. *Phys. Rev. B* **111**, 104505 (2025).
30. Gu, Y., Le, C., Yang, Z., Wu, X. & Hu, J. Effective model and pairing tendency in the bilayer Ni-based superconductor. *Phys. Rev. B* **111**, 174506 (2025).
31. Jiang, K.-Y., Cao, Y.-H., Yang, Q.-G., Lu, H.-Y. & Wang, Q.-H. Theory of pressure dependence of superconductivity in bilayer nickelate $\text{La}_3\text{Ni}_2\text{O}_7$. *Phys. Rev. Lett.* **134**, 076001 (2025).
32. Wang, B. Y., et al., Electronic structure of compressively strained thin film $\text{La}_2\text{PrNi}_2\text{O}_7$. Preprint at <https://arxiv.org/abs/2504.16372> (2025).
33. Li, P. et al. Angle-resolved photoemission spectroscopy of superconducting $(\text{La,Pr})_3\text{Ni}_2\text{O}_7/\text{SrLaAlO}_4$ heterostructures. *Natl. Sci. Rev.* nwaf205 (2025). DOI: 10.1093/nsr/nwaf205.
34. Fan, Z. et al. Superconductivity in nickelate and cuprate superconductors with strong bilayer coupling. *Phys. Rev. B* **110**, 024514 (2024).

35. Jiang, K., Wang, Z. & Zhang, F.-C. High-temperature superconductivity in $\text{La}_3\text{Ni}_2\text{O}_7$. *Chin. Phys. Lett.* **41**, 017402 (2024).
36. Xia, C., Liu, H., Zhou, S. & Chen, H. Sensitive dependence of pairing symmetry on Ni- e_g crystal field splitting in the nickelate superconductor $\text{La}_3\text{Ni}_2\text{O}_7$. *Nat. Commun.* **16**, 1054 (2025).
37. Liu, C., et al. Andreev reflection in superconducting state of pressurized $\text{La}_3\text{Ni}_2\text{O}_7$. *Sci. China-Phys. Mech. Astron.* **68**, 247412 (2025).
38. Gu, G., et al. Single particle tunneling spectrum of superconducting $\text{Nd}_{1-x}\text{Sr}_x\text{NiO}_2$ thin films, *Nat. Commun.* **11**, 6027 (2020).
39. Dynes, R. C., Garno, J. P., Hertel, G. B. & Orlando, T. P. Tunneling study of superconductivity near the metal-insulator transition. *Phys. Rev. Lett.* **53**, 2437 (1984).
40. Liu, Z. et al. Electronic correlations and partial gap in the bilayer nickelate $\text{La}_3\text{Ni}_2\text{O}_7$. *Nat. Commun.* **15**, 7570 (2020).
41. Fan, S. et al. Tunneling spectra with gaplike features observed in nickelate $\text{La}_3\text{Ni}_2\text{O}_7$ at ambient pressure. *Phys. Rev. B* **110**, 134520 (2024).
42. Li, P. et al. Photoemission evidence for multi-orbital hole-doping in superconducting $\text{La}_{2.85}\text{Pr}_{0.15}\text{Ni}_2\text{O}_7/\text{SrLaAlO}_4$ interfaces. Preprint at <https://arxiv.org/abs/2501.09255> (2025).
43. Lechermann, F., Bötzel, S. & Eremin, I. M. Low-energy perspective of interacting electrons in the normal state of superconducting bilayer nickelate. Preprint at <https://arxiv.org/abs/2503.12412> (2025).
44. Singh, D. K., Goyal, G. & Bang, Y. Possible pairing states in the superconducting bilayer nickelate. *New J. Phys.* **27**, 053503 (2025).
- 45.** Wang, Z., Zhang, G.-M., Yang, Y.-f. & Zhang, F.-C. Distinct pairing symmetries of superconductivity in infinite-layer nickelates. *Phys. Rev. B* **102**, 220501 (2020).

Figures

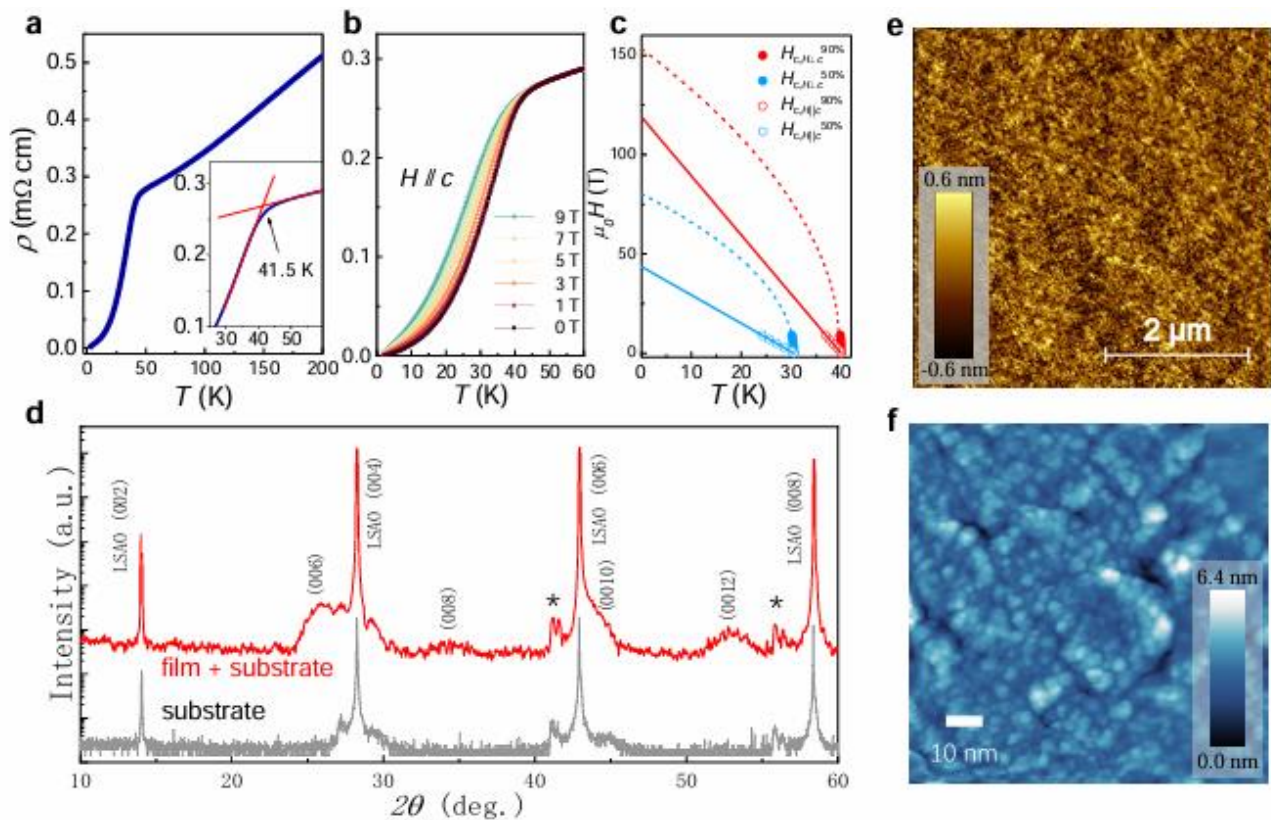


Fig. 1 | Characterization of superconducting $\text{La}_2\text{PrNi}_2\text{O}_7$ thin films. **a**, Temperature dependent resistivity of the $\text{La}_2\text{PrNi}_2\text{O}_7$ thin films. The onset transition temperature is about 41.5 K. **b**, ρ - T curves of the $\text{La}_2\text{PrNi}_2\text{O}_7$ thin film under various magnetic fields applied perpendicular to the ab plane. **c**, Temperature dependent upper critical fields extracted by the criteria of 90% $\rho_n(T)$ and 50% $\rho_n(T)$ when the magnetic field is applied perpendicular (open circles) and parallel (solid circles) to the ab plane. **d**, X-ray diffraction data of 2θ - ω scans of 2UC $\text{La}_2\text{PrNi}_2\text{O}_7$ thin film grown on SrLaAlO_4 substrate. The XRD data of the pure SrLaAlO_4 substrate are also provided for comparison. The tiny peaks marked with asterisks seem to be derived from the substrate. **e**, Atomic force microscopy image of $\text{La}_2\text{PrNi}_2\text{O}_7$ thin film with a $5 \times 5 \mu\text{m}^2$ area. **f**, Topographic image recorded by STM in an area of $100 \times 100 \text{ nm}^2$ (Setpoint conditions: $V_{\text{set}} = 8 \text{ V}$ and $I_{\text{set}} = 20 \text{ pA}$).

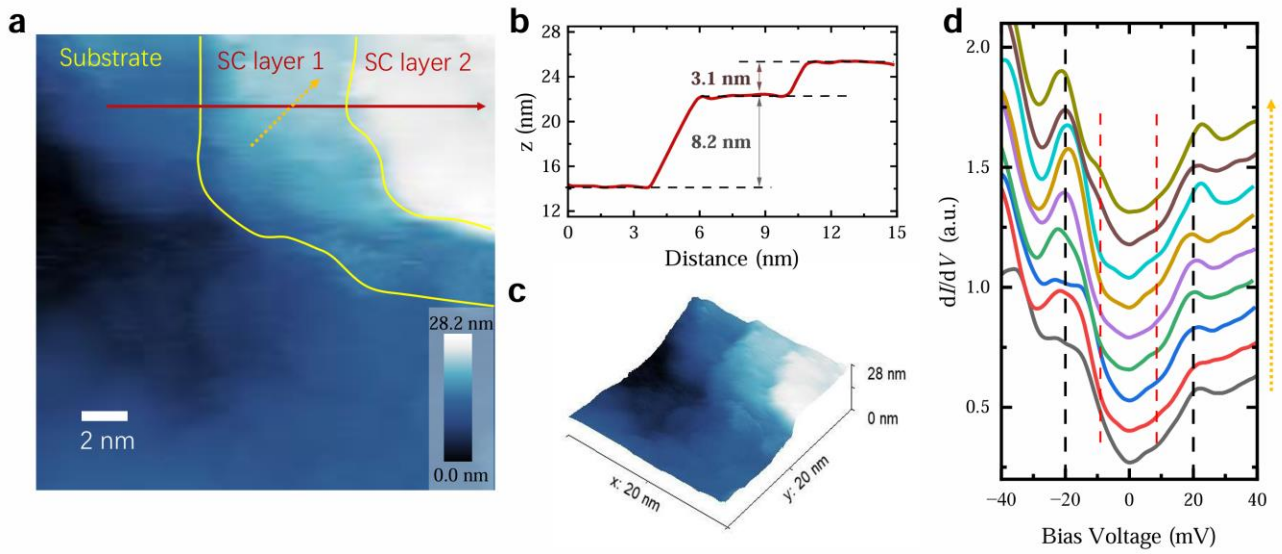


Fig. 2 | Superconducting region obtained after the tip-excitation and the tunneling spectrum. **a**, Topographic image in an area after applying a bias pulse of 2 V to the tip when it is stabilized in the initial setpoint conditions of $V_{\text{set}} = 8$ V and $I_{\text{set}} = 20$ pA. Some atomic layers of the film and even some layers of the surface substrate are removed by the operation forming some terraces. There are two terrace layers (SC layer 1 and SC layer 2) with different heights, both showing superconducting features. The two yellow lines show the rough positions of the terrace edges. **b**, Height distribution measured along the red line in **a**. The two steps correspond to different film surfaces. **c**, Three-dimensional plot of the height shown in **a**. It more clearly illustrates the height variations and the terraces. **d**, A set of tunneling spectra measured along the dotted arrowed line in SC layer 1. The spectra show the two-gap features which are illustrated by the vertical dashed lines.

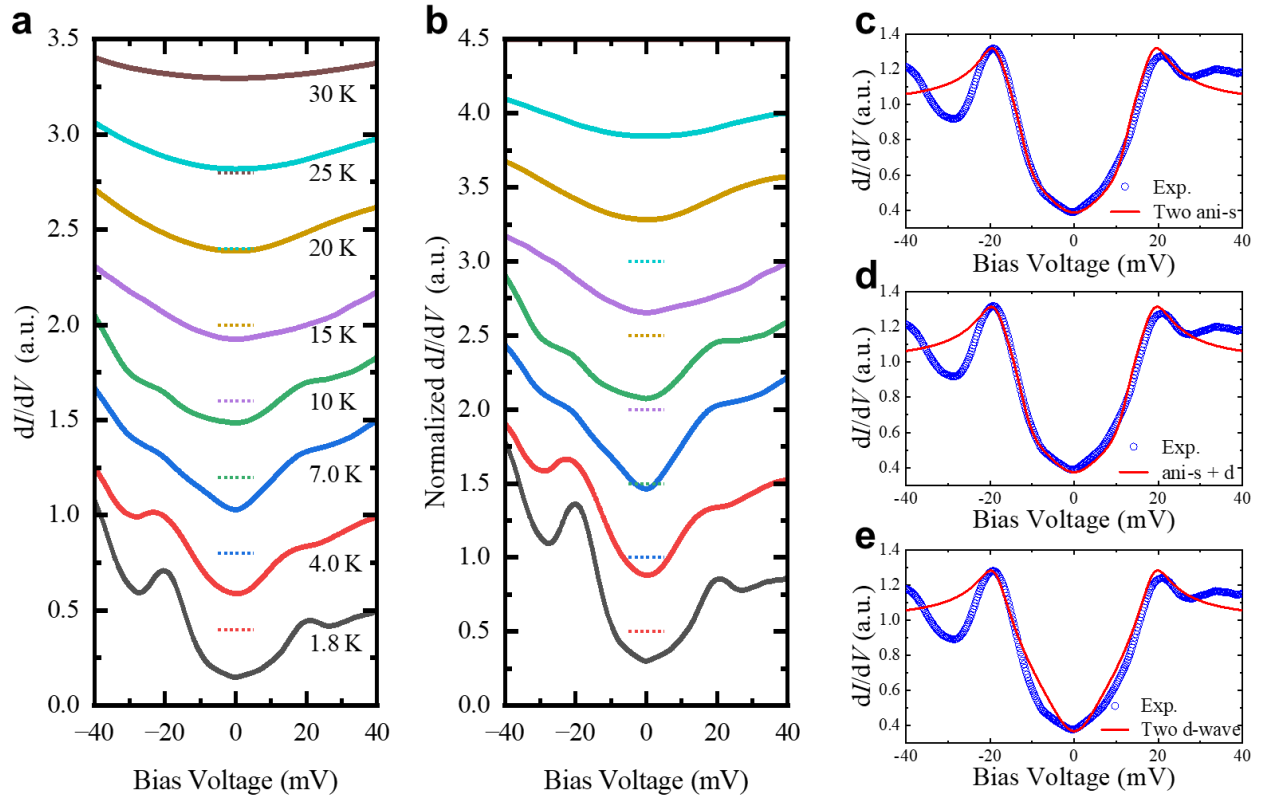


Fig. 3 | Tunneling spectra measured at different temperatures and the fitting results. a, Tunneling spectra measured at different temperatures. **b,** Tunneling spectra in **a** normalized by the spectrum measured at 30 K as the background. **c-e,** Theoretical fitting results by Dynes model with two gaps to the normalized spectrum at 1.8 K (see Extended Data Fig. 3). The gap functions used in the fittings are: **c,** $\Delta_1(\theta) = 19(0.83+0.17\cos 4\theta)$ meV, and $\Delta_2(\theta) = 6(0.8+0.2\cos 4\theta)$ meV; **d,** $\Delta_1(\theta) = 19(0.82+0.18\cos 4\theta)$ meV, and $\Delta_2(\theta) = 5.5\cos 2\theta$ meV; **e,** $\Delta_1(\theta) = 19\cos 2\theta$ meV, and $\Delta_2(\theta) = 6\cos 2\theta$ meV. Obviously, the fitting results in **c** and **d** are in good agreement with the measured spectrum, while the fitting in **e** fails to catch up main features of the experimental data.

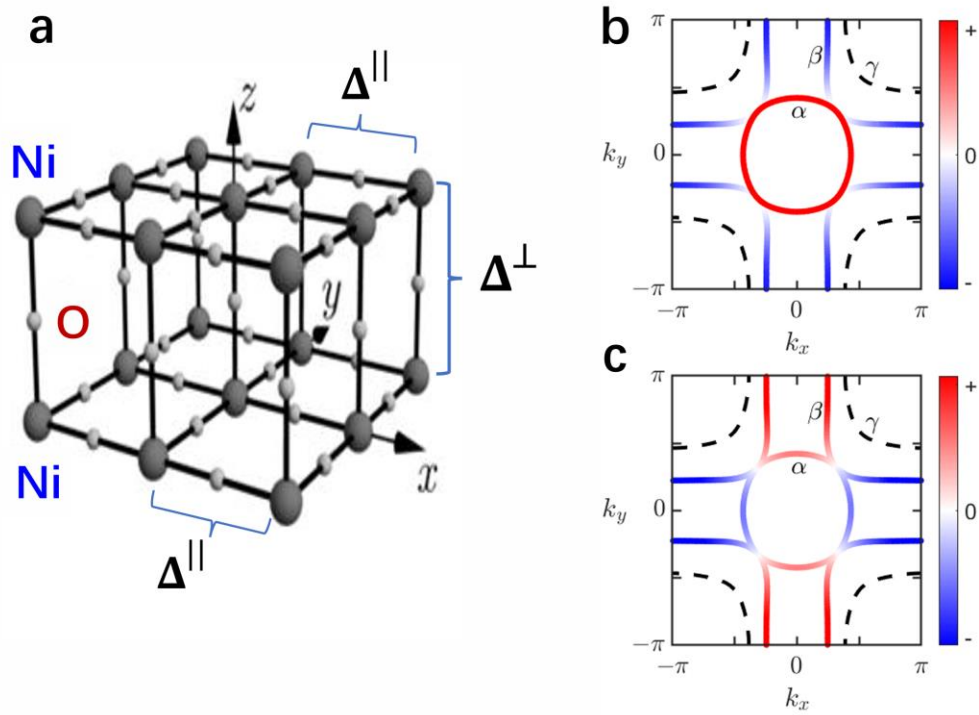
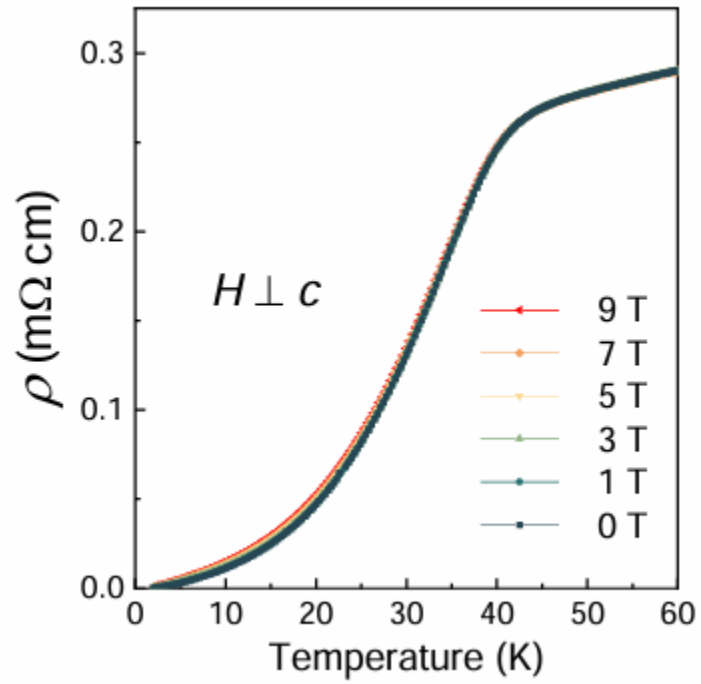
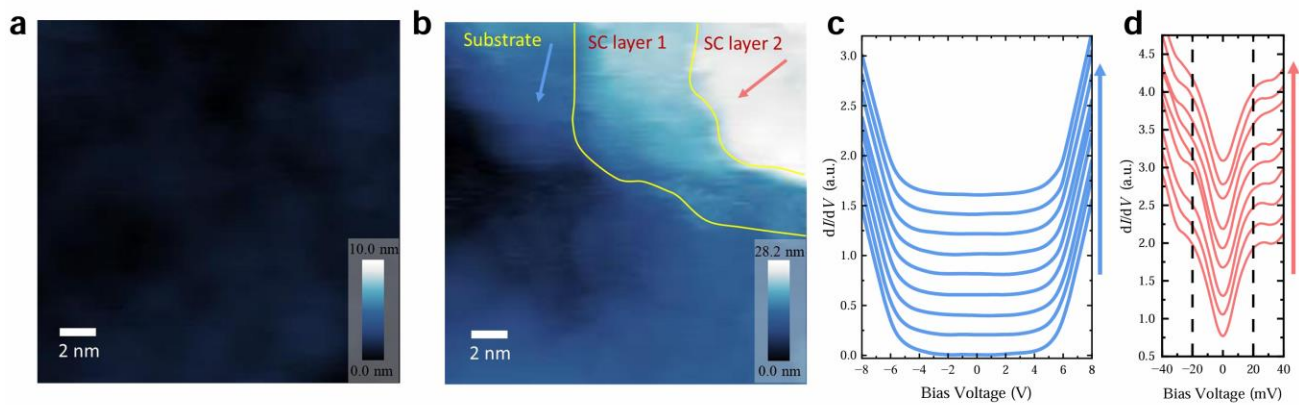


Fig. 4 | Theoretical modeling and the illustration of the superconducting gaps. a, Skeletons of the bilayer Ni-O blocks. Two NiO planes share the apical oxygen atoms. **b,c,** The Fermi surfaces and two dominant pairing models: **b** for s^{\pm} and **c** for d -wave. According to our observation and related analysis, the presence of the γ pocket at the Fermi level is not needed.

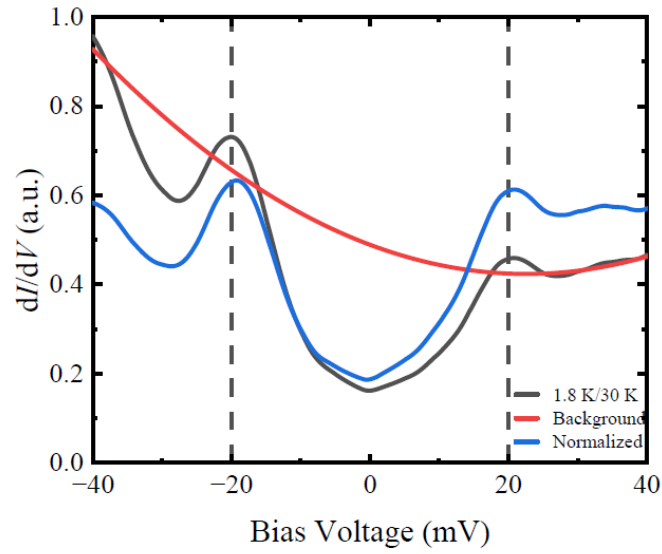


Extended Data Fig. 1 | ρ -T curves of the $\text{La}_2\text{PrNi}_2\text{O}_7$ thin film under various magnetic fields applied along the ab plane.



Extended Data Fig. 2 | Topographic image before and after the tip-excitation treatment.

a, Topographic image in an area before the tip-excitation. **b**, Topographic image in the same area after the tip-excitation. **c**, A set of tunneling spectra measured along the blue arrowed line in the substrate layer. The spectra show a very large insulating gap. (Setpoint conditions for **a** and **b**: $V_{\text{set}} = 8 \text{ V}$ and $I_{\text{set}} = 20 \text{ pA}$; for **c**: $V_{\text{set}} = 8 \text{ V}$ and $I_{\text{set}} = 100 \text{ pA}$). Here **d** shows the spectra measured on the superconducting layer 2 along the arrowed line.



Extended Data Fig. 3: Spectra before and after the subtraction of a background. After the normalization of the spectrum measured at 1.8 K by that at 30 K, there is still an inclined background. We thus fit the spectrum beyond the range of ± 35 mV with an inclined function $y = ax^2 + bx + c$, here x = bias voltage in unit of mV, $y = dI/dV$, the obtained values are $a = 1.3 \times 10^{-4}$, $b = -5.9 \times 10^{-3}$, $c = 0.49$. The obtained spectrum shows almost particle-hole symmetric behavior.

Gap notation	Δ_1 (meV)	Γ_1 (meV)	Δ_2 (meV)	Γ_2 (meV)	Δ_1 proportion
two anisotropic s-wave	19	2.6	6	6.5	65%
anisotropic s-wave + d-wave	19	2.9	5.5	5	70%
two d-wave	19	2.8	6	4	80%

Extended Data Table I | The parameters used for the Dynes model fittings in Fig. 3.

Supplementary Information for
Superconducting gaps revealed by STM measurements on
La₂PrNi₂O₇ thin films at ambient pressure

Shengtai Fan^{1†}, Mengjun Ou^{1†}, Marius Scholten^{2†}, Qing Li¹, Zhiyuan Shang¹, Yi Wang¹,
Jiasen Xu¹, Huan Yang^{1*}, Ilya Eremin^{2*}, Hai-Hu Wen^{1*}

¹ National Laboratory of Solid State Microstructures and Department of Physics, Jiangsu Physical Science Research Center, Collaborative Innovation Center of Advanced Microstructures, Nanjing University, Nanjing 210093, China.

² Institut für Theoretische Physik III, Ruhr-Universität Bochum, D-44801 Bochum, Germany

*Corresponding authors: huanyang@nju.edu.cn, Ilya.Eremin@ruhr-uni-bochum.de,
hhwen@nju.edu.cn

Supplementary Note 1: Electronic structure in a wide energy window

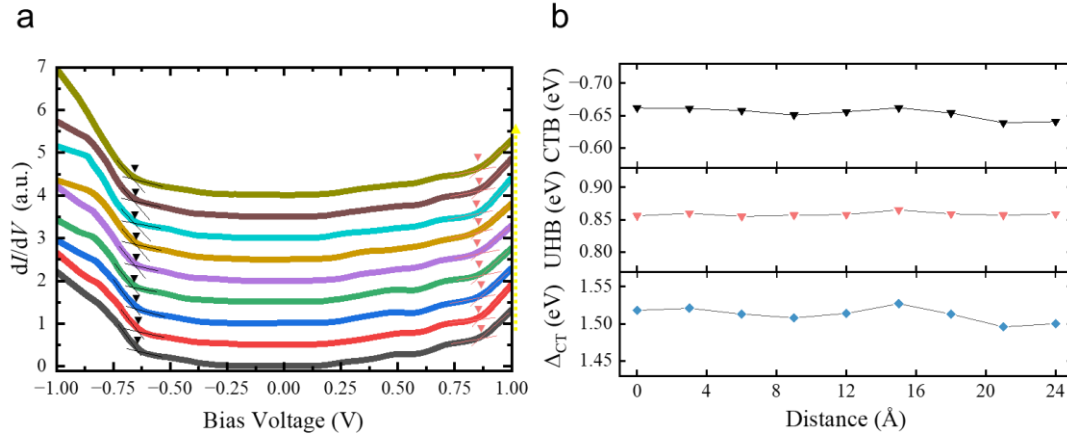
The tunneling spectra within a wide energy range from -1 V to 1 V (Supplementary Fig. 1a) were measured along the dashed arrowed line in Fig. 2a. Notably, the spectra exhibit a gap-like line shape, with the significantly suppressed spectral weights around the Fermi level and the rapid increase of spectral weights on both sides. This gap-like line shape shares similarities to those observed in doped cuprates and other doped Mott insulators, indicating that the $\text{La}_2\text{PrNi}_2\text{O}_7$ thin film may have comparable electron correlations. Recent experiments^{1,2} and corresponding theoretical calculations³ have unveiled the presence of Mottness in $\text{La}_3\text{Ni}_2\text{O}_7$. Some experiments^{4,5} and theoretical calculations^{6,7} even demonstrate the presence of charge transfer characteristics in $\text{La}_3\text{Ni}_2\text{O}_7$. Here, we use black/pink dashed lines to indicate the linear fits to the spectra below and above the charge transfer band (CTB)/upper Hubbard band (UHB), and the crossing points are determined as the onset energy of CTB/UHB. The charge transfer energy Δ_{CT} could be defined as the difference between the onset energy of UHB and CTB. The statistical analysis (Supplementary Fig. 1b) suggests the Δ_{CT} value is approximately 1.51 ± 0.05 eV, which is close to some experimental findings^{2,5} and theoretical predictions⁷ in $\text{La}_3\text{Ni}_2\text{O}_7$. Or these two edges correspond to the band edges of dense bands in that energy region.

Supplementary References

1. Liu, Z. *et al.* Electronic correlations and partial gap in the bilayer nickelate $\text{La}_3\text{Ni}_2\text{O}_7$. *Nat. Commun.* **15**, 7570 (2024).
2. Fan, S. *et al.* Tunneling spectra with gaplike features observed in nickelate $\text{La}_3\text{Ni}_2\text{O}_7$ at ambient pressure. *Phys. Rev. B* **110**, 134520 (2024).
3. Geisler, B., Hamlin, J. J., Stewart, G. R., Hennig, R. G. & Hirschfeld, P. J. Structural transitions, octahedral rotations, and electronic properties of $\text{A}_3\text{Ni}_2\text{O}_7$ rare-earth

nickelates under high pressure. *npj Quan. Mater.* **9**, 38 (2024).

4. Dong, Z. *et al.* Visualization of oxygen vacancies and self-doped ligand holes in $\text{La}_3\text{Ni}_2\text{O}_{7-\delta}$. *Nature* **630**, 847-852 (2024).
5. Chen, X. *et al.* Electronic and magnetic excitations in $\text{La}_3\text{Ni}_2\text{O}_7$. *Nat. Commun.* **15**, 9597 (2024).
6. Wú, W., Luo, Z., Yao, D.-X. & Wang, M. Superexchange and charge transfer in the nickelate superconductor $\text{La}_3\text{Ni}_2\text{O}_7$ under pressure. *Sci. China Phys., Mechan. & Astron.* **67**, 117402 (2024).
7. Chen, X., Jiang, P., Li, J., Zhong, Z. & Lu, Y. Charge and spin instabilities in superconducting $\text{La}_3\text{Ni}_2\text{O}_7$. *Phys. Rev. B* **11**, 014515 (2025).



Supplementary Fig. 1: Tunneling spectra within a wide energy range. **a**, Tunneling spectra in the energy range of ± 1.0 V measured along the dashed arrowed line in the superconducting layer 1, as shown in Fig. 2a. The black/pink symbols in **b** indicate the energy values obtained by having linear fits to the spectra near the two gap edges, and the crossing points are determined as the onset energy of the supposed CTB/UHB. Black and pink triangles mark the onset positions of CTB and UHB. **b**, The onset energy of CTB (top panel), UHB (middle panel) and the charge transfer energy Δ_{CT} (bottom panel) as a function of the measured position along the dashed arrowed line in Fig. 2a. (Setpoint conditions: $V_{set} = 1$ V and $I_{set} = 100$ pA).